Available online at www.sciencedirect.com
ScienceDirect
Trans. Nonferrous Met. Soc. China 30(2020) 1803−1815
Transactions of Nonferrous Metals Society of China
www.tnmsc.cn

Microstructure and thermophysical properties of Mg−2Zn−*x*Cu alloys

Wan-peng ZHANG[1,2,3], Ming-long MA[1,2,3], Jia-wei YUAN[1,2,3], Guo-liang SHI[1,2,3], Yong-jun LI[1,2,3], Xing-gang LI[1,2,3], Kui ZHANG[1,2,3]

1. State Key Laboratory of Nonferrous Metals and Processes, GRINM Group Co., Ltd., Beijing 100088, China;
2. GRIMAT Engineering Institute Co., Ltd., Beijing 101407, China;
3. General Research Institute for Nonferrous Metals, Beijing 100088, China

Received 3 November 2019; accepted 18 May 2020

Abstract: The microstructure and thermophysical properties of Mg−2Zn−*x*Cu alloys (*x*=0.5, 1.0 and 1.5, at.%) were investigated through microstructural and thermophysical characterization, heat treatment, and first-principles calculations. It was found that the addition of Cu had influence on the microstructure and thermophysical properties of the alloy. As the Cu content increased, the content of the MgCuZn phase increased in the as-cast alloys along with the electrical and thermal conductivities. After solution treatment, the eutectic structure partially decomposed and Zn atoms dissolved into the matrix, leading to the decrease in both the electrical and thermal conductivities of the alloy. During the early stages of the aging treatment, solute atoms precipitated from the matrix, thus increasing the electrical conductivity of the alloy. After aging for 24 h, the thermal conductivity of Mg−2Zn−1.5Cu alloy reached the maximum of 147.1 W/(m·K). The thermostable MgCuZn phases were responsible for increasing the electrical and thermal conductivities. Smaller amounts of Zn atoms dissolved in the matrix resulted in smaller lattice distortion and higher conductivities. The first-principles calculations findings also proved that the MgCuZn phases had very high conductance.

Key words: Mg−Zn−Cu alloy; heat treatment; electrical conductivity; thermal conductivity; first-principles calculations

1 Introduction

Light mass materials with efficient heat dissipation are in high demand for the continuous development of aeronautical and automotive application machines characterized by high power and fast operation speeds. Magnesium alloys with high thermal conductivity are particularly well suited for transferring heat away from the machine, increasing operational safety and the lifetime of the parts. Thermal conductivity mechanisms need to be considered when designing new alloys and developing new types of parts based on these alloys [1−3]. RUDAJEVOVÁ et al [4,5] studied the thermal diffusivity and thermal conductivity of Mg−Al-based and Mg−Sc-based alloys and found that these values decreased with increasing solute content. At room temperature, the thermal conductivity of the Mg−Al alloys ranged from 60.0 to 95.0 W/(m·K), and those for the Mg−Sc alloys ranged from 20.0 to 56.0 W/(m·K). The analysis of as-cast Mg−3Zn−(0.5−3.5)Sn alloys showed that as the Sn content in the alloys increased, their mechanical properties were improved, while the thermal conductivity decreased from 115.5 to 72.3 W/(m·K) [6]. The thermal conductivity of Mg−Zn−Mn alloys showed anisotropy [7]; for example, the thermal conductivity of the as-extruded ZM51 magnesium alloy was lower along

Foundation item: Project (51204020) supported by the National Natural Science Foundation of China; Project (BA2017044) supported by the Jiangsu Provincial Department of Science and Technology, China
Corresponding author: Ming-long MA; Tel/Fax: +86-10-60662665; E-mail: maminglong@grinm.com
DOI: 10.1016/S1003-6326(20)65340-7

the extrusion direction than that perpendicular to the extrusion direction. YING et al [8] studied the thermal conductivities of Mg−Zn and Mg−Al binary alloys and found that the decreasing effects of the thermal conductivity of Zn were negligible compared to those of Al.

Among various researched Mg alloys, Mg−Zn alloy is one of the earliest known precipitation-hardenable alloys. According to the Mg−Zn binary phase diagram, the solubility of Zn in the α-Mg matrix decreases from 2.4 at.% at the eutectic transformation temperature of 340 °C to less than 0.6 at.% at room temperature [9,10]. As Zn has a similar atomic radius to Mg, a lower lattice distortion takes place when Mg is alloyed with Zn as compared to other common alloying elements. In addition, Mg−Zn-based alloys such as ZM51, ZM61, and ZK60 have high thermal conductivity [11−13]. Cu and its alloys have been currently the most commonly used conducting materials. The characteristics of the valence electronic structure of the Cu atom result in its high electrical and thermal conductivities. Studies of typical Mg−Zn−Cu-based alloys, including ZC62, ZC63, and ZC71, have primarily focused on their structural characteristics. Some studies have reported that after heat treatment, the mechanical properties of these alloys are superior to those of Mg−Zn−Al-based alloys [14−17]. In addition, Mg−Zn−Cu-based alloys show good heat resistance and have been studied for potential applications in automotive engines that require heat resistance at both medium and high temperatures [18].

However, to date, there has only been one report of the thermal conductivity of Mg−Zn−Cu-based alloys. PAN et al [19] considered that the addition of Cu resulted in a decrease in both the amount of Zn dissolved in the matrix and the lattice distortion, which was accompanied by an increase in the electrical conductivity of the alloy. However, the authors did not discuss the influence of the eutectic structure on the electrical and thermal conductivities of the alloy [20]. Therefore, it is necessary to systematically study the effects of Cu on the thermophysical properties of Mg−Zn alloys. Developing techniques for controlling the electrical and thermal conductivities of these alloys and elucidating the mechanism governing the effect of Cu-containing compounds on their thermophysical properties can provide a theoretical background for assisting the design of new Mg-based alloys with higher thermal conductivities.

2 Experimental

The experimental alloys investigated in this study were prepared in a JDZP−25KW medium-frequency electromagnetic induction furnace using a mild steel crucible (d100 mm × H400 mm). The protective gas was a mixture of Ar (90 vol.%) and $C_2H_2F_4$ (10 vol.%). Magnesium, zinc, and copper were added as pure metals (99.95% purity). The Mg ingots were first melted in the crucible; then, Zn and Cu were added when the temperature reached 790 °C, and this temperature was maintained for 10 min. Finally, the samples were collected from the melt using a d70 mm × 75 mm stainless steel sampler and water-cooled subsequently. The actual compositions of the samples were quantified using inductively coupled plasma atomic emission spectrometry (ICP-AES), and the results are shown in Table 1.

The characterization of the microstructure was carried out using a Carl Zeiss optical microscope (Axiovert 200 MAT). The alloys were characterized using an XPERT-PRO polycrystalline X-ray diffractometer (XPert Pro MRD) with Cu K_α radiation. The generator voltage and current were set to be 40 kV and 40 mA, respectively. The scanning range was 10°−90° with a step size of 0.0330° and a time of 19.6850 s/step. Differential scanning calorimetry (DSC) curves of the as-cast alloys were obtained using a synchronous thermal analyzer (SDT Q600) with a heating rate of

Table 1 Nominal and actual compositions of Mg−2Zn− xCu (x=0.5, 1.0, 1.5, at.%) samples

Alloy	Content of Zn/at.%/wt.%		Content of Cu/at.%/wt.%		Mg
	Nominal	Actual	Nominal	Actual	
Mg−2Zn−0.5Cu	2.0/5.16	2.19/5.63	0.5/1.25	0.51/1.28	Bal.
Mg−2Zn−1.0Cu	2.0/5.12	2.14/5.46	1.0/2.49	1.01/2.52	Bal.
Mg−2Zn−1.5Cu	2.0/5.09	2.15/5.46	1.5/3.71	1.53/3.78	Bal.

10 °C/min. Back-scattered electron (BSE) images of the as-cast and as-quenched alloys were obtained using a Carl Zeiss EVO18 scanning electron microscope (SEM) coupled with an energy dispersive spectrometer (EDS). The sample morphology was observed by a transmission electron microscope (TEM; Jeol JEM−2010) with a working voltage of 200 kV after the samples were prepared by ion beam thinning (Gatan model 691). The thermal diffusivities of samples with a size of *d*12.7 mm × 2 mm were measured using a laser thermal conductivity meter (Netzsch LFA427) at room temperature. The densities of the alloys were determined using the Archimedes method. The specific heat capacities of the alloys were calculated by the Neumann−Kopp rule [21]. The thermal conductivities (TC) were calculated: $K=\alpha\rho c_p$, where α (m^2/s) is the thermal diffusivity, ρ (g/cm^3) is the density and c_p (J/(g·°C)) is the specific heat capacity at constant pressure. The electrical conductivities (EC) were measured using an eddy conductivity meter (WD-Z) at room temperature. The nanoscale conductance values of the major compounds were preliminarily calculated using first-principles methods based on the non-equilibrium Green's function within the framework of the density functional theory [22,23]. Nanodcal software (Version 20170601, Hzwtech (Shang Hai) Co., Ltd.) was used to perform the calculations.

3 Results

3.1 Microstructure and thermophysical properties of as-cast alloys

Figure 1 shows the microstructures of the as-cast Mg−2Zn−*x*Cu (*x*=0.5, 1.0, 1.5, at.%) alloys, demonstrating that they were composed of dendritic arms and eutectic structures. As the Cu content increases, the grain sizes were gradually refined, and the volume fraction of the eutectic structures continuously increased. In the alloy with 0.5 at.% Cu, the eutectic structures were distributed discontinuously along the grain boundaries (Fig. 1(a)). When the Cu content reached 1.0 at.%, the eutectic structures of the alloy changed to a continuous network morphology, and the dendritic arms showed a petal-like structure (Fig. 1(b)). When the Cu content reached 1.5 at.%, the eutectic structure was gradually coarsened and the grain sizes were further refined. The solid solubility of Cu in α-Mg is extremely low, reaching a maximum of 0.013 at.% at the eutectic temperature. With further increase in the Cu content, additional alloying elements precipitated at the front of the solid−liquid interface, resulting in constitutional supercooling and accelerated nucleation, leading to grain refinement.

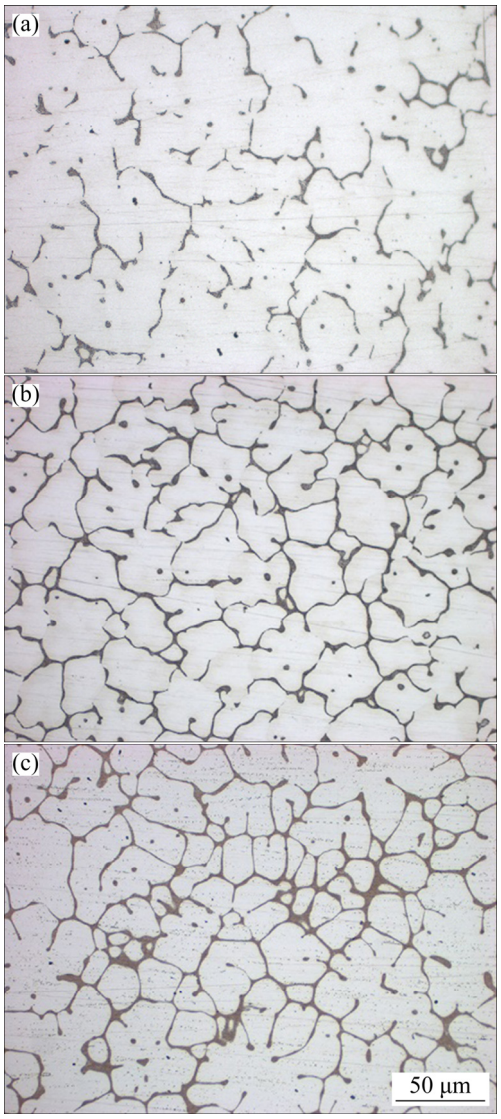

Fig. 1 OM images of as-cast Mg−2Zn−*x*Cu alloys: (a) *x*=0.5 at.%; (b) *x*=1.0 at.%; (c) *x*=1.5 at.%

Figure 2 presents the XRD patterns of the as-cast Mg−2Zn−*x*Cu (*x*=0.5, 1.0, 1.5, at.%) alloys. These alloys consisted primarily of α-Mg and MgCuZn phases. According to International Centre for Diffraction Data (ICDD; PDF No. 65−7003), the structure of the MgCuZn phase crystallizes in a cubic system with a lattice constant of *a*=0.7169 nm, and a space group of $Fd\bar{3}m$. In contrast, WANG et al [24] analyzed the phase of as-cast Mg−6Zn−*x*Cu

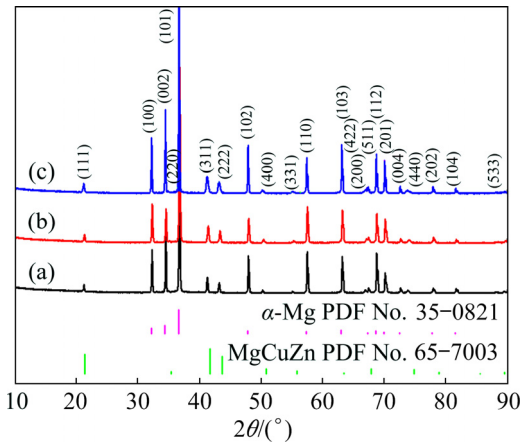

Fig. 2 XRD patterns of as-cast Mg−2Zn−*x*Cu alloys: (a) *x*=0.5 at.%; (b) *x*=1.0 at.%; (c) *x*=1.5 at.%

alloy using XRD and identified a secondary tetragonal CuMgZn phase with lattice constants of *a*=0.5069 nm and *c*=0.7169 nm, and the space group of $P\bar{4}$ (ICDD; PDF No. 41−0778). From the experimental results obtained in this study, the order of the intensities of the three strongest XRD peaks was consistent with that of the MgCuZn phase and different from that of the CuMgZn phase. The differences in the Cu content and cooling rates may explain the differences between the findings of the previous study and our current results. The theoretical Cu contents presented in Ref. [24] were (1.0−5.0) wt.%, while the Cu contents in our work were (1.28−3.78) wt.% ((0.5−1.5) at.%). In addition, air cooling was used in the previous study after die casting, while water cooling was used here as it has a faster cooling rate.

SEM images of the as-cast alloys are shown in Fig. 3, showing that the eutectic structure had a lamellar morphology. As the Cu content increased, the volume fraction of the eutectic structures increased, and the interlamellar spacing became smaller because of the constitution and temperature supercooling. The volume fractions of the eutectic

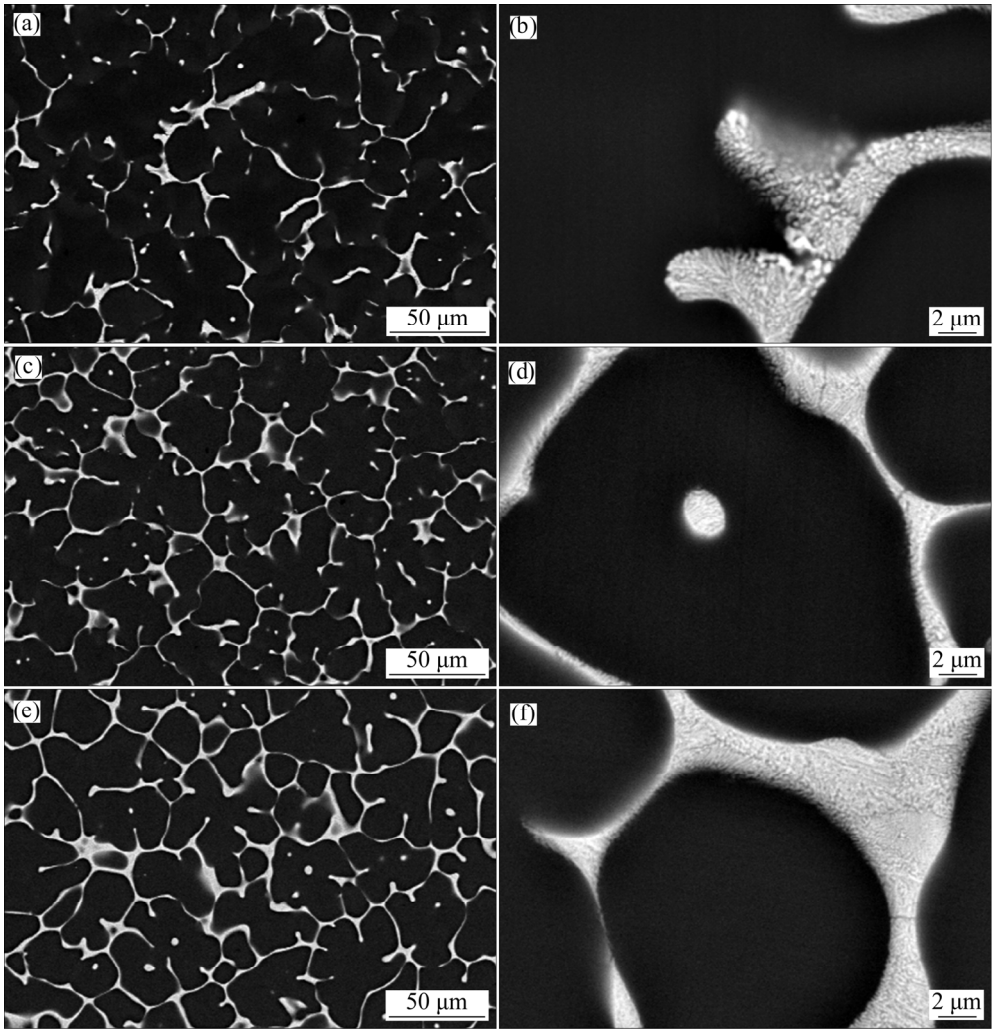

Fig. 3 SEM images of as-cast Mg−2Zn−*x*Cu alloys: (a, b) *x*=0.5 at.%; (c, d) *x*=1.0 at.%; (e, f) *x*=1.5 at.%

structures in these three alloys were 6.6%, 8.3%, and 13.0% for alloys with 0.5, 1.0, and 1.5 wt.% Cu, respectively.

Figure 4 displays the EDS results of the as-cast alloy matrix (Fig. 4(a)) and the eutectic structure (Fig. 4(b)). As Cu was added, the Zn content in the matrix increased slightly, while the Cu content in the matrix remained nearly unchanged. In the eutectic microstructure, the Cu content gradually increased, and the Zn content and the Zn/Cu molar ratio decreased gradually. In the equilibrium solidification process, the solid solubility of Zn decreased from 2.4 at.% to <0.5 at.% in the Mg−Zn binary alloy. In an actual non-equilibrium solidification process, because of the high cooling rate, it is impossible for solute atoms to precipitate strictly according to the solid solubility curve of the phase diagram. Therefore, a certain amount of Zn and Cu remained in the matrix. Moreover, the solidus temperature increased with increasing Cu content, along with the hardness. As a result, a high amount of Zn dissolved into the matrix rather than precipitating out as a part of the eutectic structure.

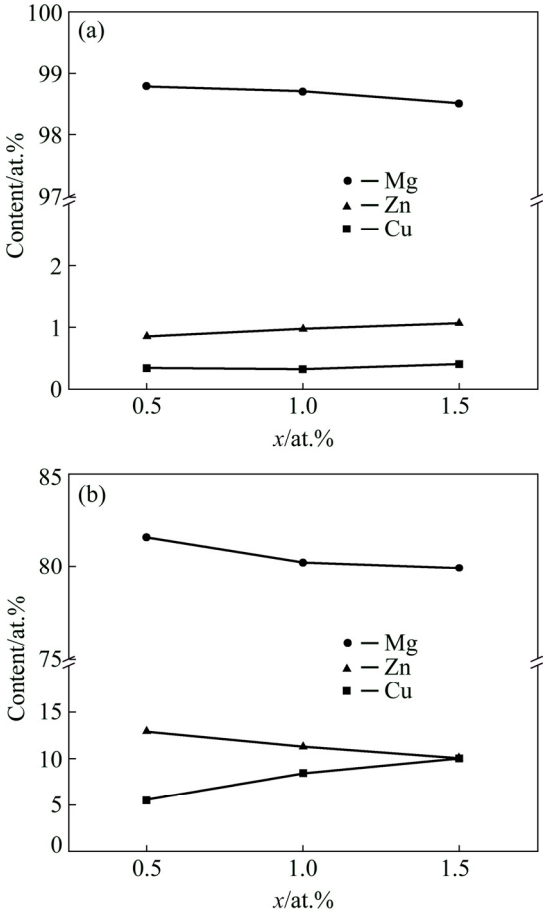

Fig. 4 EDS results of as-cast Mg−2Zn−*x*Cu alloys: (a) Matrix; (b) Eutectic structure

Therefore, the Zn/Cu ratio in the eutectic structure gradually decreased with increasing Cu content.

Figure 5(a) presents TEM image of the as-cast Mg−2Zn−1.5Cu alloy. This figure showed that the eutectic structure of the alloy had a skeletal morphology. The selected area electron diffraction pattern (SAED, Fig. 5(b)) showed that the phase had a cubic structure with a lattice constant of a=0.7093 nm, which was approximately equal to that of the MgCuZn phase (ICDD; PDF No. 65−7003). In Figs. 5(c) and (d), the molar ratio of the secondary phase was Mg:Cu:Zn= 32.21:37.17:30.62, which was close to a ratio of 1:1:1.

Figure 6 shows the electrical and thermal conductivities of the as-cast alloys. Both values increased with increasing Cu content. The electrical conductivity of the 1.0 at.% Cu alloy increased by 2.7% compared with that of the 0.5 at.% Cu alloy, whereas the electrical conductivity of the 1.5 at.% Cu alloy increased by 1.2% compared with that of the 1.0 at.% Cu alloy. Moreover, the average thermal conductivities of the alloys with 0.5, 1.0, and 1.5 at.% Cu were 124.4, 132.6, and 141.4 W/(m·K), respectively.

DSC curves of the as-cast alloys are shown in Fig. 7. The extrapolated onset temperatures of the second phase were between 455 and 459 °C, and the temperatures of the endothermic peak were between 461 and 463 °C. In addition, the endothermic peak area increased with increasing Cu content, and the heat capacities were 13.20, 27.60 and 33.04 J/g. According to Refs. [25,26], the alloys were severely oxidized at 445 °C; however, after heating the temperature to 430 °C, the alloys did not appear to be significantly oxidized. Based on these investigations, the condition of the solid solution treatment process was set to be 430 °C and held for 24 h.

3.2 Microstructure and thermophysical properties of as-quenched alloys

The XRD patterns of the as-quenched Mg−2Zn−*x*Cu (x=0.5, 1.0, 1.5 at.%) alloys are shown in Fig. 8. The alloys were primarily composed of the α-Mg matrix and MgCuZn phase.

Figure 9 shows SEM images of the as-quenched alloys, revealing that the eutectic structure of the alloy was partially dissolved and the remaining un-dissolved secondary phases were

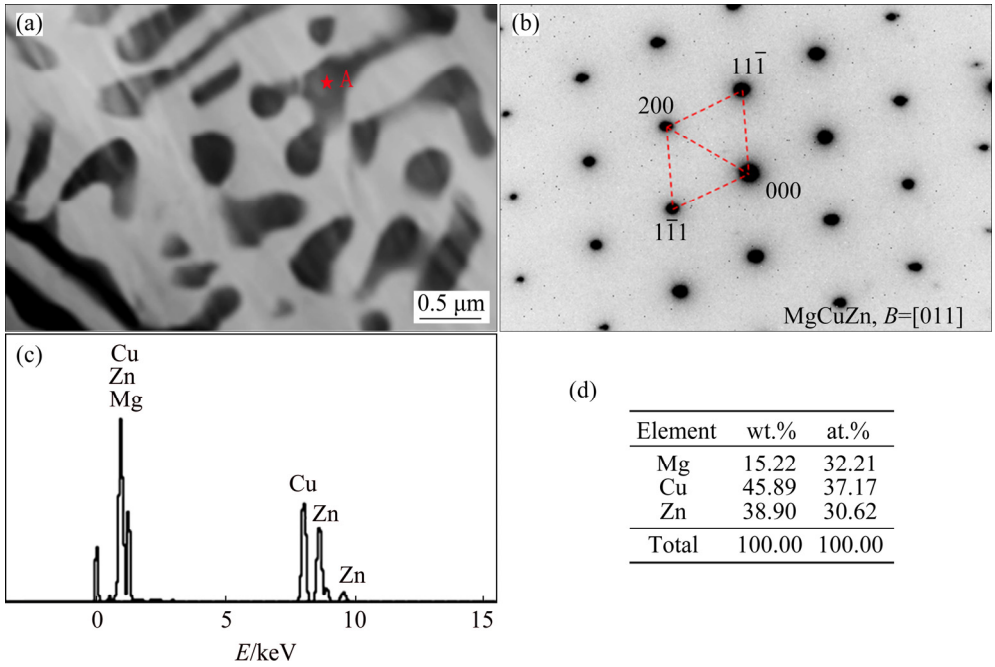

(d)

Element	wt.%	at.%
Mg	15.22	32.21
Cu	45.89	37.17
Zn	38.90	30.62
Total	100.00	100.00

Fig. 5 Bright-field TEM image of as-cast Mg−2Zn−1.5Cu alloy (a), SAED pattern (b) and EDS results (c, d) of MgCuZn

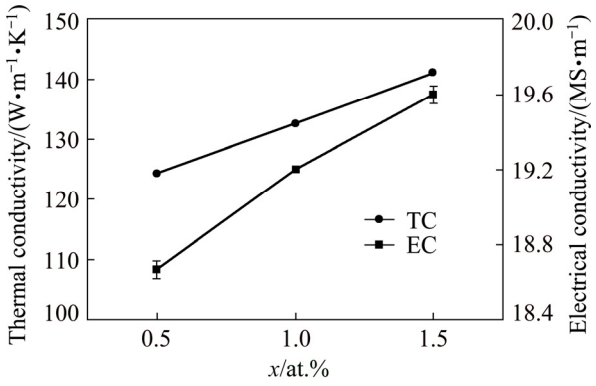

Fig. 6 Electrical and thermal conductivities of as-cast Mg−2Zn−*x*Cu alloys

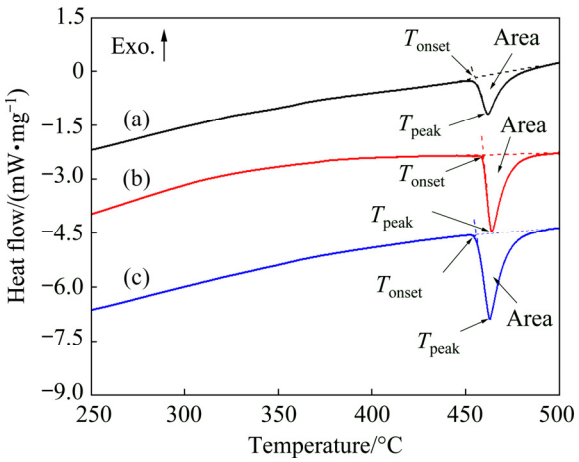

Fig. 7 DSC curves of as-cast Mg−2Zn−*x*Cu alloys: (a) *x*=0.5 at.%; (b) *x*=1.0 at.%; (c) *x*=1.5 at.%

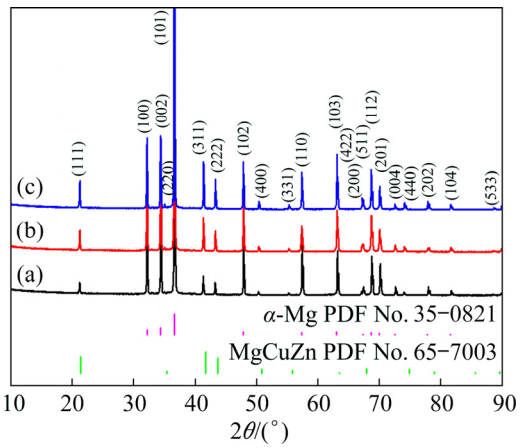

Fig. 8 XRD patterns of as-quenched Mg−2Zn−*x*Cu alloys: (a) *x*=0.5 at.%; (b) *x*=1.0 at.%; (c) *x*=1.5 at.%

intermittently distributed along the grain boundaries in a spherical morphology. The comparison of Figs. 9(a), (c), and (e) revealed that the volume fraction of the remaining secondary phases increased with increasing Cu content, while the secondary phases gradually changed from island-like structure to chain-like structure. In addition, as shown in Figs. 9(b), (d), and (f), the layered shape of the secondary phases in the as-quenched alloys completely disappeared.

Figure 10 shows the EDS results of the as-quenched alloy matrix (Fig. 10(a)) and the undissolved secondary phases (Fig. 10(b)).

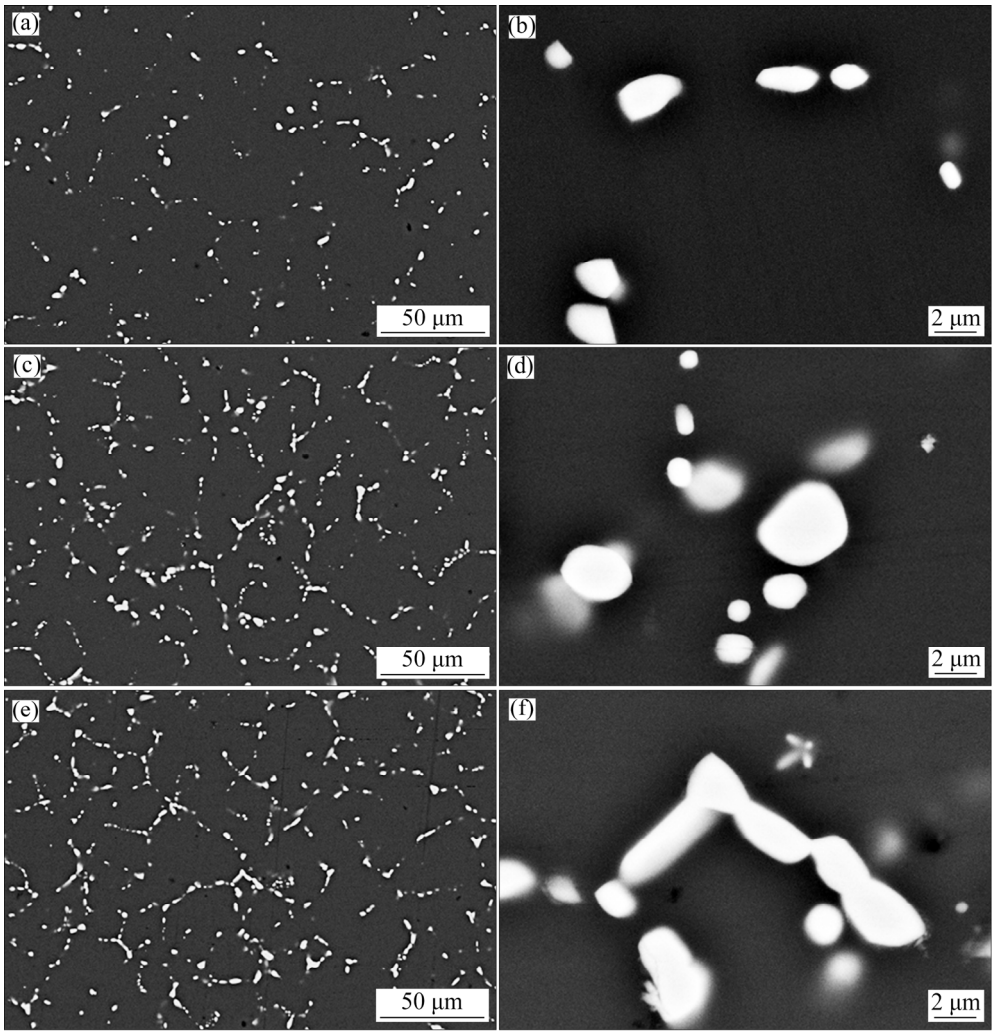

Fig. 9 SEM images of as-quenched Mg−2Zn−*x*Cu alloys: (a, b) *x*=0.5 at.%; (c, d) *x*=1.0 at.%; (e, f) *x*=1.5 at.%

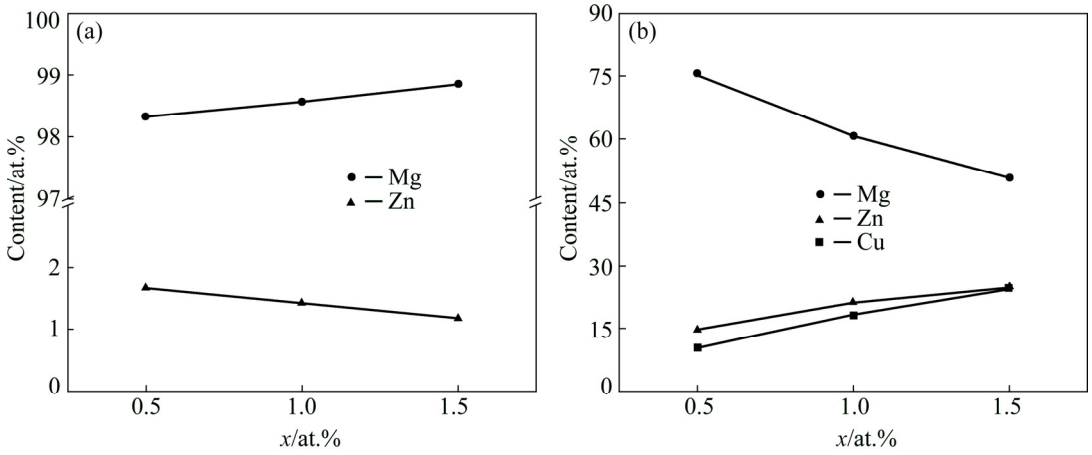

Fig. 10 EDS results of as-quenched Mg−2Zn−*x*Cu alloys: (a) Matrix; (b) Eutectic structure

Figure 10(a) shows that the Zn content in the matrix of the as-quenched alloy was higher than that of the as-cast alloy, and decreased with increasing Cu content. The formation of the MgCuZn phase consumed Zn which might have otherwise been dissolved in the matrix. As shown in Fig. 10(b), the contents of Zn and Cu in the as-quenched alloys were higher than those in the as-cast alloys, where the Zn/Cu molar ratio approached 1:1, due to the weaker segregation after

the solution treatment.

Figure 11 shows bright-field TEM image of the as-quenched Mg−2Zn−1.5Cu alloy and SAED pattern of the undissolved secondary phase MgCuZn. The size of the spherical secondary phase was approximately 1 μm (Fig. 11(a)). According to the SAED pattern (Fig. 11(b)), this phase had a cubic structure with a lattice constant of a= 0.7096 nm, similar to the results obtained for the as-cast alloy.

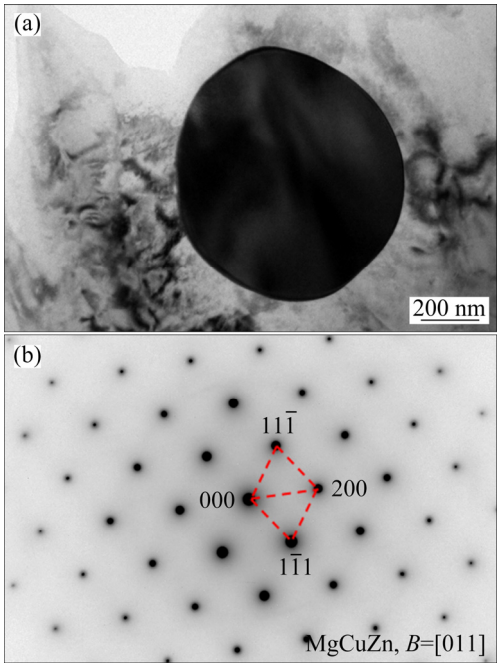

Fig. 11 Bright-field TEM image of as-quenched Mg−2Zn−1.5Cu alloy (a), and SAED pattern of MgCuZn (b)

Figure 12 compares the electrical and thermal conductivities of the as-cast and as-quenched alloys, where both alloys exhibited identical trends in the conductivity data with increasing Cu content. After solution treatment, the electrical and thermal conductivities of the as-quenched alloys decreased compared with those of the as-cast alloys.

3.3 Microstructures and thermophysical properties of aged alloys

Figure 13 shows the electrical conductivities of Mg−2Zn−xCu (x=0.5, 1.0, 1.5 at.%) alloys aged at 160 °C for 0−50 h. The electrical conductivities of the alloys increased rapidly during the initial aging stage and the alloy with 0.5 at.% Cu showed the fastest increase in the curve. The electrical conductivity of the alloy increased slightly at 6 h and then fluctuated within a narrow range before finally stabilizing.

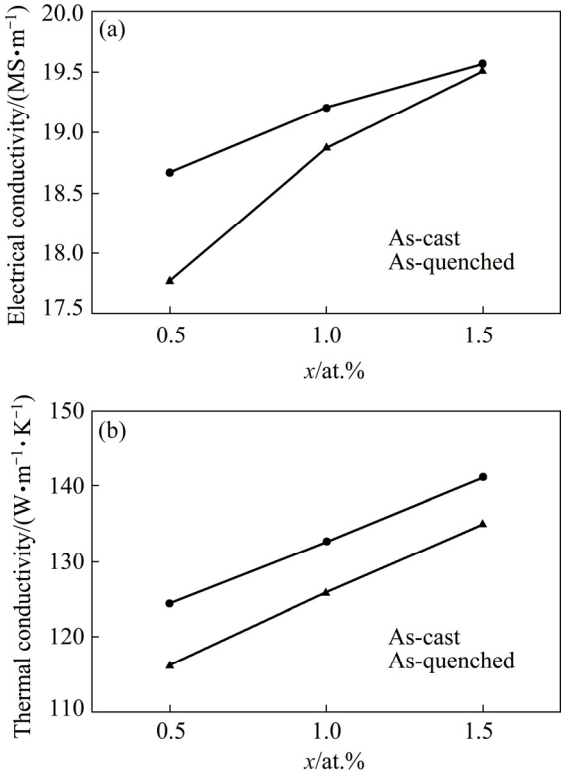

Fig. 12 Electrical (a) and thermal (b) conductivities as function of Cu content for as-cast and as-quenched Mg−2Zn−xCu alloys

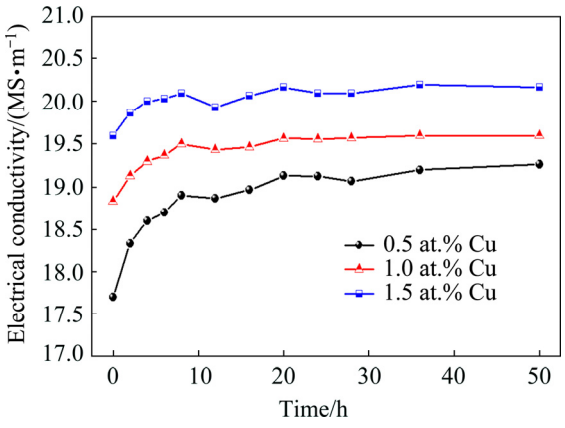

Fig. 13 Electrical conductivity variation of as-quenched Mg−2Zn−xCu alloys (x=0.5, 1.0, and 1.5 at.%) aged at 160 °C for 0−50 h

The alloys with 1.5 at.% Cu were characterized using TEM after aging for 6 and 24 h. As shown in Figs. 14(a, b), after the aging treatment, fine lamellar precipitates with 2−5 nm in size were randomly distributed in the matrix. BUHA and OHKUBO [27] and BUHA [28] considered a similar region as a Guinier−Preston (GP) zone,

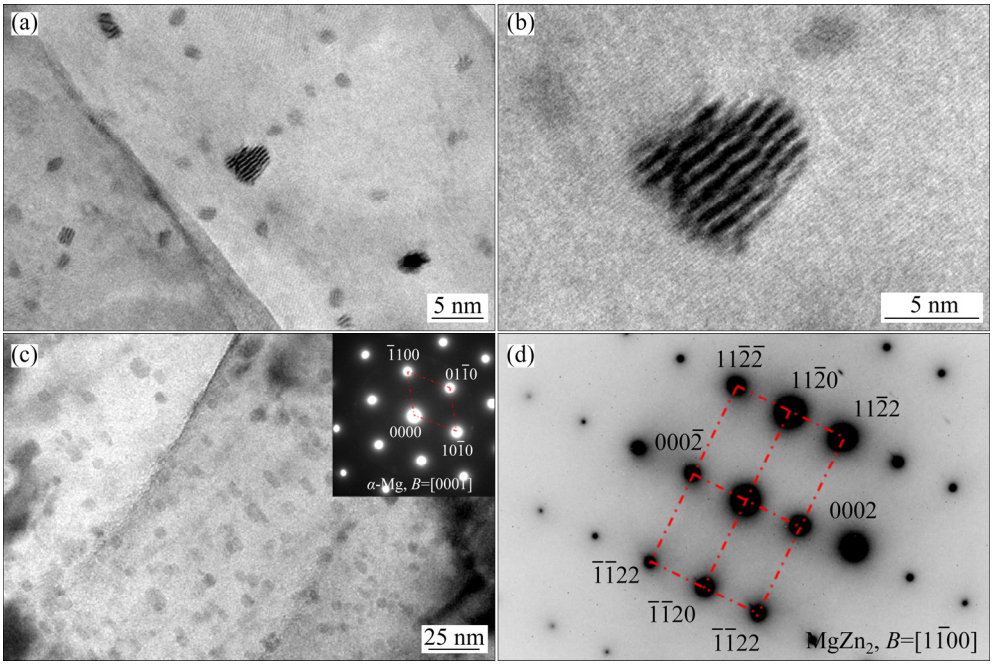

Fig. 14 TEM images of aged Mg−2Zn−1.5Cu alloys: (a, b) Bright-field images (6 h); (c, d) Bright-field TEM image and SAED pattern (24 h), respectively

which had a hexagonal structure and a completely coherent relationship with the matrix. As shown in Figs. 14(c, d), the precipitates in the matrix clearly grew after 24 h of aging treatment, becoming a hexagonal system with lattice constants of a=0.50 nm and c=0.82 nm; this indicated a hexagonal close-packed $MgZn_2$ phase, with precipitates of 5−20 nm in size.

The thermal conductivity values increased after 24 h of aging treatment, for both the as-cast and as-quenched alloys (as shown in Fig. 15). On one hand, solute atoms precipitate during the aging treatment, which reduces the scattering of electrons by phonons. On the other hand, heat treatment can reduce casting stress and relieve lattice distortion. Therefore, the aged alloys have the highest thermal conductivity among the materials studied here. In particular, the thermal conductivity of the aged alloy with 1.5 at.% Cu reaches the maximum value of 147.1 W/(m·K).

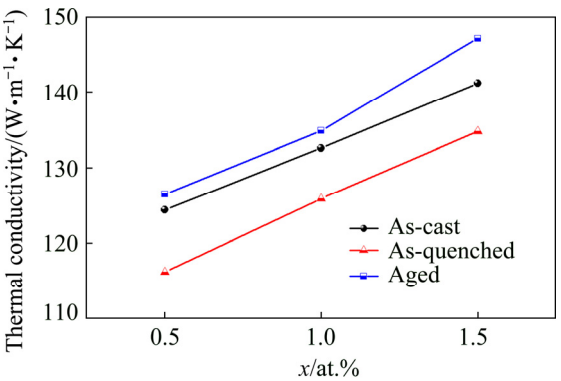

Fig. 15 Thermal conductivity as function of Cu content of as-cast, as-quenched and aged (24 h) Mg−2Zn−xCu alloys

4 Discussion

Generally, the electrical and thermal conductivities of an alloy are lower than those of pure metal. A perfect crystal has a well-ordered lattice and the transport of electrons and phonons is completely unhindered. However, once alloying elements are added, both the solid solution and the secondary phases will cause lattice shrinkage or expansion, resulting in lattice distortion that can hinder such movements. This phenomenon occurs particularly when the difference in atomic radii between the solute atom and the matrix atom is very large [29,30].

The primary factors that affect the thermal conductivity of the as-cast alloys in this study were the solute atoms in the matrix, the grain size, and the presence of intermetallic compounds (IMCs). In general, the solute atoms dissolved in the matrix can reduce both the electrical and thermal conductivities of the alloys. Furthermore, smaller

grain sizes can increase the electron and phonon scattering interfaces, which also reduces the electrical and thermal conductivities of the alloy. IMCs tend to have low conductivity, which can deteriorate the thermophysical properties of the alloy. Higher fractions of the MgCuZn phase formed with increasing Cu content, which was the most important IMC in these alloys. However, both the electrical and thermal conductivities of the alloys increased with increasing Cu content. Note that the addition of Cu did not lead to a decrease in the Zn content in the matrix (Fig. 4(a)). Additionally, as the Cu content increased, the grain size of the as-cast alloy decreased, while the grain boundary area increased accordingly. It can be sure that both of them limited the electrical and thermal conductivities of the alloy. Hence, the presence of MgCuZn phases is most likely the main reason for improving both the electrical and thermal conductivities of the material. The electrical conductivity of pure Cu is 2.6 times higher than that of pure Mg, and the thermal conductivity of pure Cu is 2.5 times higher than that of pure Mg. According to the energy band theory, the electrons in the s-orbital of the valence shell of Cu are conduction electrons, indicating that Cu is a good conductor because the valence band is only half full. Therefore, the MgCuZn phase, which contains a large number of Cu atoms, may provide a greater number of free electrons and preferential transport channels for heat transfer and show higher heat conduction efficiency compared with Cu-free IMCs. Moreover, the addition of Cu can promote the occupancy of vacancies by solute atoms, thus reducing the number of microscopic defects in the alloy [15,24]. As a result, the scattering of electrons and phonons is reduced, which contributes to improving the electrical and thermal conductivities of the alloys.

Currently, relevant thermophysical data for the MgCuZn phase have remained scarce, and there have been no reports on the electrical and thermal conductivities of this phase. To predict the conductance of the MgCuZn phase, first-principles calculations were performed here based on the nonequilibrium Green's function method within the framework of density functional theory [22,23]. In addition, the conductance values of pure Mg and $MgZn_2$ phases were calculated as a parallel control test. Figure 16 shows the schematic diagram of the simulated lattices with unit cells of Mg, MgCuZn, and $MgZn_2$. The numerical results presented that the conductance of per unit area of pure Mg, MgCuZn, and $MgZn_2$ were 9.85, 5.06, and 6.12×10^{-24} G_0/nm^2 ($G_0\approx7.75\times10^{-5}$ Ω^{-1}), respectively, which indicated that the conductance per unit area of the MgCuZn phase was several orders of magnitude higher than that of the $MgZn_2$ phase. Hence, the electrical conductivity of the MgCuZn phase is much higher than that of the $MgZn_2$ phase. Although there may be additional factors that were not considered here, our basic methods and principles were consistent with those of preliminary numerical calculation [31]. The addition of Cu reduced the content of the $MgZn_2$ phase. The simulated results further confirmed that, with the addition of Cu, the increasing fraction of MgCuZn phases increased the electrical and thermal conductivities of the alloys. Moreover, with the addition of Cu, the grain size decreased and the eutectic structures formed a network-like morphology, which can also provide preferential heat transfer channels.

After solution treatment, the electrical and thermal conductivities of the alloys decreased compared with those of the as-cast alloys. As previously mentioned, the increased solute atoms in the matrix would lead to a stronger scattering of electrons and phonons. In addition, the alloy was immediately water-cooled after solution treatment, which formed a large number of vacancies. The interaction between the vacancies and electrons was another reason for the reduction in the electrical and thermal conductivities. Considering atomic radii, when Zn (R_{Zn}=0.1379 nm) is dissolved in the matrix (R_{Mg}=0.1598 nm), the lattice of the surrounding matrix shrinks and electrons and phonons are strongly scattered, thus reducing their mean free paths [29]. In addition, the scattering interactions between electrons and phonons reduce the electron energy below the Fermi level, implying that the carrier density, and hence, electrical and thermal conductivities decrease.

In the early stage of aging, solute atoms precipitate from the matrix, which promotes the conduction of electrons and phonons and increases the overall electrical conductivity. During aging, the electrical conductivity of the alloy tends to fluctuate, a phenomenon that may be caused by the appearance of GP zones [19]. As shown in

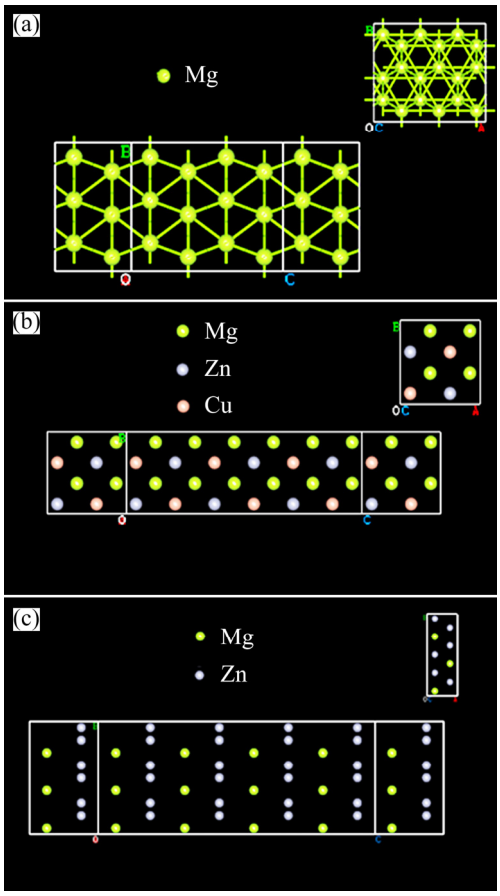

Fig. 16 Schematic diagrams of conductance model: (a) Mg; (b) MgCuZn; (c) $MgZn_2$

Figs. 14(a, b), after aging treatment for 6 h, such GP zones were observed by TEM. On one hand, the interface of the GP zones is in a coherent relationship with the matrix, leading to increased lattice distortion. On the other hand, the sizes of the GP zones are of the same order of magnitude as the mean free path of free electrons, causing significant interference by electron vibrations which can reduce both the mean free path of electrons and the electrical conductivity of the alloys. Over a prolonged aging time, the solute atoms precipitate continuously, and the secondary phases increase in size and number. After 24 h aging treatment, the precipitates greatly increased in size and became $MgZn_2$ phases that were in a non-coherent relationship with the matrix. The electrical conductivity of the alloy increased and then tended to stabilize. Moreover, based on the trends of the electrical and thermal conductivities of the alloys in other states, these results are in accordance with the Wiedemann–Franz law [29].

In conclusion, the electrical and thermal conductivities of Cu-containing Mg−Zn alloys are closely related to the properties of the IMCs. The thermophysical properties of the MgCuZn phase can play a key role in the behavior of the alloy. Although heat treatment can change the morphology of the MgCuZn phase, it cannot change basic physical properties of the MgCuZn phase. Moreover, the DSC curves of the alloys indicated that it is difficult for the MgCuZn phase to decompose due to its high melting temperature and high thermal stability. Therefore, Cu-containing Mg−Zn-based alloys are expected to be excellent heat-resistant magnesium alloys for engineering applications.

5 Conclusions

(1) The eutectic structures of the as-cast Mg−2Zn−xCu (x=0.5, 1.0, 1.5, at.%) alloy are composed of α-Mg and MgCuZn phases (cubic structure with a lattice constant of a=0.7093 nm measured by TEM). As the Cu content increases, the eutectic structures gradually change from discontinuous spherical shape to a continuous coarse network, while the grain size of the as-cast alloys decreases accordingly. Both the electrical and thermal conductivities of the as-cast alloys increase with increasing Cu content due to the high conductivity of the MgCuZn phase and the network formed by the eutectic structures, which provide preferential heat transfer channels.

(2) After solution treatment, the eutectic structures of the as-cast alloys partially dissolve and change to necklace-like structures. The electrical and thermal conductivities of the as-quenched alloys decrease compared with those of the as-cast alloys.

(3) GP zones form in the matrix during the early stage of aging. As the aging proceeds, these zones transform into $MgZn_2$ phase. The electrical conductivity of the alloys also increases as the aging process proceeds, while the aged alloys show the highest electrical and thermal conductivities. The maximum thermal conductivity of 147.1 W/(m·K) is close to that of the pure Mg.

Acknowledgments

The authors would also like to thank professor Li-gen WANG, doctor Wei XIAO, and doctor Lun-wei YANG of the GRIMAT Engineering

Institute Co., Ltd., for their help with the simulations.

References

[1] WANG Qiang, ZHANG Zhi-min, ZHANG Xing, LI Guo-jun. New extrusion process of Mg alloy automobile wheels [J]. Transactions of Nonferrous Metals Society of China, 2010, 20(S2): s599−s603.

[2] CHRISTENSEN A, GRAHAM S. Thermal effects in packaging high power light emitting diode arrays [J]. Applied Thermal Engineering, 2009, 29(2−3): 364−371.

[3] KULEKCI M K. Magnesium and its alloys applications in automotive industry [J]. International Journal of Advanced Manufacturing Technology, 2008, 39(9−10): 851−865.

[4] RUDAJEVOVÁ A, STANĚK M, LUKÁC P. Determination of thermal diffusivity and thermal conductivity of Mg−Al alloys [J]. Materials Science and Engineering A, 2003, 341(1−2): 152−157.

[5] RUDAJEVOVÁ A, BUCH F V, MORDIKE B L. Thermal diffusivity and thermal conductivity of MgSc alloys [J]. Journal of Alloys and Compounds, 1999, 292(1−2): 27−30.

[6] WANG Chun-ming, CHEN Yun-gui, XIAO Su-fen, DING Wu-cheng, LIU Xia. Thermal conductivity and mechanical properties of as-cast Mg−3Zn−(0.5~3.5)Sn alloys [J]. Rare Metal Materials and Engineering, 2013, 42(10): 2019−2022.

[7] YUAN Jia-wei, ZHANG Kui, LI Ting, LI Xing-gang, LI Yong-jun, MA Ming-long, LUO Ping, LUO Guang-qiu, HAO Yong-hui. Anisotropy of thermal conductivity and mechanical properties in Mg−5Zn−1Mn alloy [J]. Materials & Design, 2012, 40: 257−261.

[8] YING T, ZHENG M Y, LI Z T, QIAO X G, XU S W. Thermal conductivity of as-cast and as-extruded binary Mg−Zn alloys [J]. Journal of Alloys and Compounds, 2015, 621: 250−255.

[9] NIE J F, MUDDLE B C. Characterisation of strengthening precipitate phases in a Mg−Y−Nd alloy [J]. Acta Materialia, 2000, 48(8): 1691−1703.

[10] NIE Jian-feng. Precipitation and hardening in magnesium alloys [J]. Metallurgical and Materials Transactions A, 2012, 43(11): 3891−3939.

[11] PAN Hu-cheng, PAN Fu-sheng, PENG Jian, GOU Jun, TANG Ai-tao, WU Lu, DONG Han-wu. High-conductivity binary Mg−Zn sheet processed by cold rolling and subsequent aging [J]. Journal of Alloys and Compounds, 2013, 578: 493−500.

[12] YUAN Jia-wei, ZHANG Kui, ZHANG Xu-hu, LI Xing-gang, LI Ting, LI Yong-jun, MA Ming-long, SHI Guo-liang. Thermal characteristics of Mg−Zn−Mn alloys with high specific strength and high thermal conductivity [J]. Journal of Alloys and Compounds, 2013, 578: 32−36.

[13] SHI G L, ZHANG D F, ZHANG H J, ZHAO X B, QI F G, ZHANG K. Influence of pre-deformation on age-hardening response and mechanical properties of extruded Mg−6%Zn−1%Mn alloy [J]. Transactions of Nonferrous Metals Society of China, 2013, 23(3): 586−592.

[14] YAMASAKI M, KAWAMURA Y. Thermal diffusivity and thermal conductivity of Mg−Zn-rare earth element alloys with long-period stacking ordered phase [J]. Scripta Materialia, 2009, 60(4): 264−267.

[15] LI Xiao, LIU Jiang-wen, LUO Cheng-ping. Precipitation behavior of cast ZC62 magnesium alloy [J]. Acta Metallurgica Sinica, 2006, 42(7): 733−738. (in Chinese)

[16] GOLMAKANIYOON S, MAHMUDI R. Microstructure and creep behavior of the rare-earth doped Mg−6Zn−3Cu cast alloy [J]. Materials Science and Engineering A, 2011, 528(3): 1668−1677.

[17] ZHU Hong-mei, LUO Cheng-ping, LIU Jiang-wen, JIAO Dong-ling. Growth twinning behavior of cast Mg−Zn−Cu−Zr alloys [J]. Transactions of Nonferrous Metals Society of China, 2014, 24(2): 316−320.

[18] POLMEAR I J. Magnesium alloys and applications [J]. Materials Science and Technology, 1994, 10(1): 1−16.

[19] PAN H C, PAN F S, WANG X, PENG J, SHE J, ZHAO C, HUANG Q, SONG K, GAO Z Y. High conductivity and high strength Mg−Zn−Cu alloy [J]. Materials Science and Technology, 2014, 30(7): 759−764.

[20] ZHANG Wan-peng. Effect of Cu element on microstructure and thermophysical properties of Mg−Zn alloy [D]. Beijing: State Key Laboratory of Nonferrous Metals and Processes, General Research Institute for Nonferrous Metals, 2018: 20−60. (in Chinese)

[21] LEITNER J, VOŇKA P, SEDMIDUBSKÝ D, SVOBODA P. Application of Neumann–Kopp rule for the estimation of heat capacity of mixed oxides [J]. Thermochimica Acta, 2010, 497(1−2): 7−13.

[22] GUO H, TAYLOR J, WANG J. Ab initio modeling of moleculear electronics: Transport properties of C60 molecular junction and carbon nanotube-metal interfaces [C]//Proceedings of the APS Meeting. Washington DC, USA: American Physical Society, 2001: A20.013.

[23] WALDRON D, HANEY P, LARADE B, MACDONALD A, GUO H. Nonlinear spin current and magnetoresistance of molecular tunnel junctions [J]. Physical Review Letters, 2006, 96(16): 166804.

[24] WANG Peng-fei, HUANG Xiao-feng, FENG Kai, ZHANG Shao-hui, LI Xiang-ping. Study on microstructure and mechanics properties of as-cast Mg−6Zn−*x*Cu alloys [J]. China Foundry Machinery & Technology, 2012(1): 10−13. (in Chinese)

[25] YUAN Jia-wei, LI Xing-gang, ZHANG Kui, LI Ting, LI Yong-jun, MA Ming-long, SHI Guo-liang, LI Meng. Influence of heat treatment on microstructure and mechanical properties of die-cast AZ91D alloy with RE elements [J]. Applied Mechanics and Materials, 2014, 633−634: 98−102.

[26] MA Ming-long, ZHANG Kui, LI Xing-gang, LI Yong-jun, ZHANG Kang. Homogenization heat treatment of GWN751K magnesium alloy [J]. The Chinese Journal of Nonferrous Metals, 2010, 20(1): 1−9. (in Chinese)

[27] BUHA J, OHKUBO T. Natural aging in Mg−Zn(−Cu) alloys [J]. Metallurgical & Materials Transactions A, 2008, 39(9): 2259−2273.

[28] BUHA J. Natural ageing in magnesium alloys and alloying with Ti [J]. Journal of Materials Science, 2008, 43(4): 1220−1227.

[29] KITTEL C, HELLWARTH R W. Introduction to solid state physics [J]. Physics Today, 1957, 10(6): 43−44.
[30] YANG Ji-hui. Thermal conductivity—Theory, properties and applications [M]. New York: Kluwer Academic/Pleneum Publishers, 2004: 2−26.
[31] OLIVER D J, MAASSEN J, OUALI M E, PAUL W, HAGEDORN T, MIYAHARA Y, QI Y, GUO H, GRÜTTER P. Conductivity of an atomically defined metallic interface [J]. Proceedings of the National Academy of Sciences of the United States of America, 2012, 109(47): 19097−19102.

Mg−2Zn−*x*Cu 合金的显微组织和热物性能

张万鹏[1,2,3]，马鸣龙[1,2,3]，袁家伟[1,2,3]，石国梁[1,2,3]，李永军[1,2,3]，李兴刚[1,2,3]，张 奎[1,2,3]

1. 有研科技集团有限公司 有色金属材料制备加工国家重点实验室，北京 100088；
2. 有研工程技术研究院有限公司，北京 101407；
3. 北京有色金属研究总院，北京 100088

摘 要：通过显微组织和热物性能表征、热处理及第一性原理计算，研究 Mg−2Zn−*x*Cu (*x*=0.5, 1.0, 1.5，摩尔分数，%) 合金的显微组织和热物性能。结果表明，添加 Cu 元素对合金显微组织和热物性能有影响。随着 Cu 含量增加，铸态合金中 MgCuZn 相含量增加，铸态合金电导率和热导率增大。固溶处理后，合金中共晶组织部分溶解，Zn 原子回溶进入基体，导致合金的电导率和热导率均降低。时效处理前期，溶质原子从基体中沉淀析出，合金电导率增大，时效 24 h 后，Mg−2Zn−1.5Cu 合金的热导率最高达到 147.1 W/(m·K)。合金中形成的热稳定 MgCuZn 相对合金的电导率和热导率起促进作用。Zn 元素在基体中含量越低，晶格畸变程度越低，导热性能则越好。另外，第一性原理计算结果也表明 MgCuZn 三元相具有很好的导电和导热性能。

关键词：Mg−Zn−Cu 合金；热处理；电导率；热导率；第一性原理计算

(Edited by Wei-ping CHEN)